PCCP

Accepted Manuscript

ROYAL SOCIETY OF CHEMISTRY

rsc.li/pccp

View Article Online
DOI: 10.1039/C7CP01971H

Journal Name

ARTICLE

Direct Experimental Observation of Mesoscopic Fluorous Domains in Fluorinated Room Temperature Ionic Liquids

Received 00th January 20xx,
Accepted 00th January 20xx

DOI: 10.1039/x0xx00000x

www.rsc.org/

F. Lo Celso[a,f], Y. Yoshida[b], F. Castiglione[c], M. Ferro[c], A. Mele[c,d], C. J. Jafta[e], A. Triolo[f,*] and O. Russina[g]

Fluorinated room temperature ionic liquids (FRTILs) represent a class of solvent media that is attracting great attention due to the IL-specific properties as well as features stemming from their fluorous nature. Medium-to-long fluorous tails constitute a well-defined apolar moiety in the otherwise polar environment. Similarly to the case of alkyl tails, such chains are expected to deliver the formation of self-assembled fluorous domains. So far, however, no direct experimental observation could be done of the existence of such structural heterogeneities at the nm scale. We report here the first experimental evidence of the existence of mesoscopic spatial segregation of fluorinated domains, on the basis of highly complementary X-ray and neutron scattering data sets (highlighting the importance of the latter probe) and NMR spectroscopy. Data are interpreted using atomistic Molecular Dynamics simulations, emphasizing the existence of a self-assembly mechanism that delivers segregated fluorous domains, where preferential solubilisation of fluorinated compounds can occur, thus paving the way to several smart applications.

Introduction

Fluorinated compounds represent a technologically relevant class of materials[1]. They possess peculiar properties that make them attractive for a wide variety of fields including surfactants[2,3], bio-medicine[4,5], biphasic (bio-)catalysis[6–12] and synthesis[13–18], gas absorption[4,19–21] etc. Selectively functionalised compounds with fluorinated moieties might then play a major role in acting as interfaces between fluorous and more conventional solvents aiming at contacting otherwise immiscible media. In this respect fluorinated room temperature ionic liquids (FRTILs, or FILs, when melting point is above RT) are attracting great attention in the last few years, as they show several interesting properties that are inherited from both their ionic and fluorinated nature. For example, recently a first review contribution showed the relevance of FILs in addressing several high impact fields, such as recovery of fluorinated compounds, CO_2 capturing and biomedical applications. [22] Therein, mention was made to the first reports describing the synthesis of FILs [23,24] and the peculiar features of this class of ionic compounds, as compared to their equivalent non fluorous counterparts. Aiming at developing task-specific ILs with specific activity triggered by appropriate functionalisation, Davis and co-workers prepared a series of imidazolium based ILs bearing two side chains, one of them being fluorinated.[24] This kind of FIL has been studied by different groups that aimed for example to describe structural and other kind of properties using a merging of experimental and computational techniques [25–30] Other ILs containing fluorous moieties have been proposed later on (see e.g. [31–34]). More recently different investigations focused on ILs containing fluorinated anions [22,34–51]. Among these studies some focused on symmetric bis(perfluoroalkanesulfonyl)-amide $(C_nF_{2n+1}SO_2)_2N$ anions (hereinafter indicated as $[IM_{xx}]$, where x corresponds to the perfluoro alkyl chain length), paired with the diethylmethyl(2-methoxyethyl)ammonium (hereinafter indicated as [DEME]) cation. ILs based on the latter cation have been investigated in several studies [52–58], while the symmetric anions bearing long fluoroalkyl chain have been less carefully investigated [45,47,48,51,59].

The systematic investigation by one of the authors explored a series of RTILs bearing [DEME] cation and different $[IM_{xx}]$ anions, with $0 \le x \le 4$.[45] Most ILs exhibit negligible vapor pressure owing to Coulombic interactions between component ions. In addition, ionic liquids bearing $[IM_{xx}]$ anions are thermally stable relative to those composed of other inorganic anions such as Cl and PF_6 [60]; namely, they can provide a wider liquid region. In general, ammonium-based ionic liquids are more

[a] Dipartimento di Fisica e Chimica, viale delle Scienze, ed. 17, 90128 Palermo, Italy.
[b] Faculty of Agriculture, Meijo University, Nagoya 468-8502, Japan.
[c] Department of Chemistry, Materials and Chemical Engineering "G. Natta", Politecnico di Milano, Piazza L. da Vinci 32, - 20133 Milano, Italy
[d] CNR ICRM Istituto di Chimica del Riconoscimento Molecolare Via L. Mancinelli, 7 - 20131 Milano, Italy
[e] Soft Matter and Functional Materials, Helmholtz-Zentrum für Materialien und Energie GmbH, Berlin, Germany
[f] Laboratorio Liquidi Ionici, Istituto Struttura della Materia, Consiglio Nazionale delle Ricerche, Rome, Italy
[g] Department of Chemistry, University of Rome Sapienza, Rome, Italy

Electronic Supplementary Information (ESI) available: Scheme 1 representing molecular structures and atom numbering for cation and anions of the ILs used in this work. See DOI: 10.1039/x0xx00000x

View Article Online
DOI: 10.1039/C7CP01971H

resistant against oxidation and reduction compared with imidazolium-based ionic liquids, while keeping the anion constant [61,62]. Among ammonium-based cations, the [DEME] cation has a relatively low molecular symmetry for its low molecular weight (or size). This results in its high ion-diffusivity, i.e., high ionic conductivity and low viscosity of the ionic liquids [45]. For these reasons, it is obvious that [DEME][IM_{xx}] are among the best ionic liquids for application to electrochemical devices. In fact, thanks to its commercial availability, much efforts have been devoted to study [DEME][IM_{11}] as an alternative to conventional organic solvents for diverse devices such as lithium ion batteries [63], electric double-layer capacitors [64,65], and field-effect transistors [66]. In particular, [DEME][IM_{11}] has already been put into practical use as the electric double-layer capacitor, which is now expected to be loaded onto hybrid electric vehicles.

In this scenario, we aimed at exploring the role of perfluoroalkyl chain length in affecting the mesoscopic organisation of the [DEME][IM_{xx}] RTILs. Previous studies, both experimental and computational, by Greaves et al. [35] and Margulis et al. [36] evidenced that ILs bearing a fluorous anion with long enough perfluoroalkyl tail are characterised by a distinct low Q peak in their X-ray scattering pattern. This evidence was rationalised in terms of the mutual segregation of alkyl and perfluoroalkyl tails that tend to self-exclude themselves and self-assemble into alkyl and fluorous domains. On the other hand it was acknowledged in refs. [35,36] that the existence of a strong hydrogen bond correlation between opposite ionic species in the system under study (that also raised notably the IL's melting point above room conditions) can be well considered as a driving force towards the self-exclusion and segregation of the two different kinds of alkyl chains. In a related study, some of us showed that a series of RTILs (that are liquid at ambient conditions and behave as good ILs) bearing the asymmetric fluorinated anion [IM_{14}] are characterised by an essentially featureless X-ray diffraction pattern at room conditions, but develop a distinct low Q peak, associated to the segregation of the fluorous tails, when decreasing temperature.[43] That was a first indication of fluorous domains in RTILs; on the other hand the fingerprint of such a domains formation could be detected only below 250 K. Potential evidences of such a fluorous domains formation could have been obtained in recent studies of RTILs based on symmetric fluorinated anions: Castner et al. reported the X-ray scattering pattern from an RTIL with the 1-methyl-3-trimethylsilylpropylimidazolium cation and the [IM_{22}] anion at ambient temperature[47]; Mezger et al. reported X-ray and neutron scattering patterns over a limited Q range on a series of long alkyl chain imidazolium based ILs, namely [C_{18}mim][IM_{44}] and [C_{22}mim][IM_{44}] at temperatures above 330 K (above the ILs' s melting points)[48]. In both cases however only the low Q peak associated to the long side alkyl chain could be detected without providing indication on the existence of segregated fluorous domains. Such an indication was provided for the case of RTILs (i.e. ILs with melting points at or below ambient conditions) by the research activity of Canongia-Lopes and coworkers on the basis of computational studies[38,39,51,67], without, however, providing a direct experimental evidence of the existence of such a kind of structural heterogeneity that can be expected to manifest a large impact on technological applications. Driven by this puzzling situation, we undertook the study of the sample series [DEME][IM_{xx}] as a function of the fluorous side chain length, aiming at detecting the existence of structural heterogeneities related to the segregation of fluorous tails. Here we reveal the outstanding role played by the synergic use of X-ray and neutron scattering in revealing the experimental fingerprint of fluorous domains existence. These experimental evidences are further supported by NMR experiments and rationalised at the atomistic level using state of the art Molecular Dynamics simulations. Very recently Ferreira and coworkers presented experimental (thermal analysis and rheological properties) and computational findings on a series of FILs and FRTILs, bearing fluorinated anions and in particular on [pyr_{14}][IM_{44}], where [pyr_{14}] corresponds to 1-butyl-N-methylpyrrolidinium[51]. For these samples they computed the neutron scattering pattern out of their MD simulation, providing simulation results in agreement with the experimental findings that we report herein.

Experimental Details.

[DEME][IM_{xx}] ILs ($0 \leq x \leq 4$) were synthesised by the metathesis of [DEME]Br and A[IM_{xx}] (A: alkali metal cation) in aqueous solution. [45]. The chemical structure and the atom numbering is shown in Scheme 1 in the Supplementary Information.

X-ray scattering. Small and Wide X-ray Scattering (SWAXS) experiments were conducted at the 11-ID-C beamline at the Advanced Photon Source, Argonne National Laboratory. Measurements were conducted using an X-ray wavelength of 0.11165 Å. CeO_2 was used as a calibrant. Samples were inserted into 2 mm diameter quartz capillaries and maintained at ambient temperature during the whole course of the measurements (typically between 20 and 40 minutes). Empty capillary contribution was subtracted and various corrections including detector sensitivity and Compton scattering were applied using the PDFgetX2 software.[68]

Small Angle Neutron Scattering. Small Angle Neutron Scattering experiments (SANS) measurements were performed at the small-angle scattering instrument V4 which is placed in the cold neutron guide of Helmholtz-Zentrum Berlin (HZB). The magnitude of the scattering vector is defined as $Q = (4\pi/\lambda)(\sin\theta)$ with λ being the wavelength and 2θ the scattering angle. The measured neutron flux of the V4 is ~10^6 $cm^{-2}.s^{-1}$ for the wavelength used, λ = 4.5 Å.[69] The scattering data was obtained at one sample detector distance of 1.0 m, which yields a total momentum transfer range of 0.5 $nm^{-1} < Q < 8$ nm^{-1}. For further information regarding the V4 instrument and its resolution the reader is referred to references [69,70]. The samples were placed into circular quartz cuvettes with inner spacing of 1 mm and placed in the beam for measurement. A Cd aperture of 13 mm was used for the scattering measurements. The 2D scattering data was reduced to a scattering curve ($d\Sigma/d\Omega(Q)$ vs. Q; hereinafter indicated as I(Q) vs Q) by means of the BerSANS software. The raw data is then

View Article Online
DOI: 10.1039/C7CP01971H

corrected for transmission, the quartz cell background scattering subtracted and converted to absolute units taking into account the scattering from water.[71]

NMR spectroscopy. The ^{1}H and ^{19}F NMR spectra were acquired on a Bruker Avance 500 spectrometer operating at the 500.13 MHz proton frequency equipped with a QNP four nuclei switchable probe. The IL samples (0.5-1.0 g each)–were transferred in a 5 mm NMR tube and subsequently dehydrated overnight under dynamic vacuum (mechanical pump), then the tube was immediately flame-sealed. A co-axial capillary containing DMSO-d6 was used as internal reference. The ^{19}F spectrum of DEME44 sample was acquired with a sweep width of 68 ppm and relaxation delay of 5 s. Homonuclear {^{19}F-^{19}F} Nuclear Overhauser Effect Spectroscopy (NOESY) experiments were acquired with a sweep width of 68 ppm, 8 scans for each experiment and 700 increments in the t1 dimension. Several spectra were acquired with NOE mixing time in the range 50 ms – 1 s. Heteronuclear {^{1}H-^{19}F} HOESY experiments were performed using the inverse-detected pulse sequence [72] with 400 increments in the t1 dimension and sixteen scans for each experiment. Thirteen experiments were performed with mixing times in the range 20 ms – 1.2 s. The 2D data sets were processed with SI2=2K points and SI1=512 points. Squared cosine bell window multiplication was then applied in both dimensions before 2D Fourier transform. The cross-peak integrals were measured using the Bruker software. The peak volume of each cross-peak has been corrected by considering the contribution of the number of spins. The cross-peak intensity arising from N_I equivalent spins I (^{1}H) and N_S equivalent spin S (^{19}F) is proportional to the ratio of $N_IN_S/(N_I + N_S)$; [73] therefore, for semi-quantitative comparison, the original peak volume has been corrected by dividing the original integral by the value $N_IN_S/(N_I + N_S)$. For all the experiments, the temperature was set and controlled at 300 K.

The spectra were processed with Topspin software (Bruker, version 3.5) The HOESY build-up curve were drawn plotting the normalized integral of the heteronuclear cross peak versus the mixing time (τ). Quantitative NOEs were extracted by double-exponential fitting of the experimental curves according to Eq. 1 [74] and after checking the assumption that R, the total relaxation rate, is equal for all H and F nuclei:

$$NOE_H\{F\}(\tau) = \frac{1}{2}e^{-(R-\sigma_{HF})\tau}(1 - e^{-2}\sigma_{HF}\tau) \quad (1)$$

Computational details.

Molecular dynamic simulations were performed using the GROMACS 5.1.1 package [75,76]. Interactions were described using an all-atoms potential [77–81]. The simulations were performed using a cubic box of 1000 ion pairs, where periodic boundary conditions were applied. Force field parameter files and initial configuration were created using the DLPGEN software ([82] and http://webpages.fc.ul.pt/~cebernardes/dlpgen_prog/Software_dlpgen.html (accessed on 02.03.2017)). The equilibration procedure consisted of several steps, starting from a series of NPT simulations at high temperatures, using scaled partial charges, followed by progressive lowering of the temperature and increasing of the charges to their final value until an equilibrated system was obtained at 298.15 K and 1 bar, after a 15 ns run. After the mentioned equilibration phase, the system was run for further 15 ns, and then the trajectory of the last 5 ns was saved at a frequency of 1 ps for calculation of the structural properties. The simulations were always checked versus the experimental density and the energy profile. For the temperature coupling, we used a velocity rescaling thermostat[83] (with a time coupling constant of 0.1 ps), while for the pressure coupling, we used a Parrinello–Rahman barostat [84] (1 ps for the relaxation constant). The Leap-Frog algorithm with a 1 fs time step was used for integrating the equations of motion. Cut-offs for the Lennard- Jones and real space part of the Coulombic interactions were set to 15 Å. For the electrostatic interactions, the Particle Mesh Ewald (PME) summation method[85,86] was used, with an interpolation order of 6 and 0.08 nm of FFT grid spacing. Selected graphs were done using Matplotlib[87]. Weighted structure factors were computed by using in-house developed software, accordingly to text book formulas as highlighted in recent Margulis's work[88].

Results and Discussion.

Melting points for some of [DEME][IM_{xx}] ILs are just below 20°C; nevertheless all of the samples can be referred to as RTILs. Moreover, even upon rapid cooling (e.g. 50 K min^{-1}), no glassy or super-cooled liquid state could be obtained for samples with x>1, thus indicating the tendency of these symmetric anions to stabilise the crystalline phases. In reference [45], it was appreciated that the melting points for the [DEME][IM_{xx}] series grow with the elongation of the perfluoroalkyl chain in the anions, thus indicating a role played by van der Waals interactions between these tails in determining the ILs' melting points.

The experimental Small- and Wide-Angle X-ray Scattering (S-WAXS) patterns from the [DEME][IM_{xx}] series at ambient conditions are shown in Figure 1. It can be appreciated that

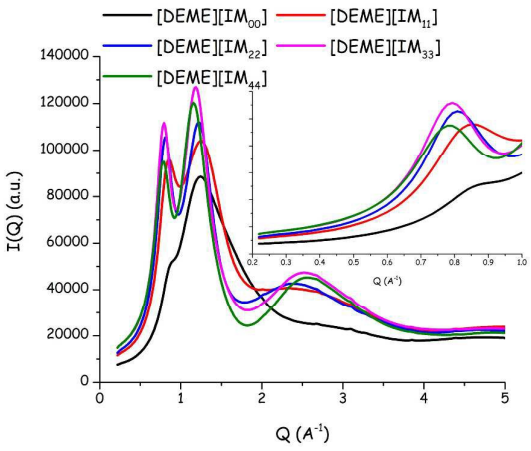

Figure 1. S-WAXS data from the series of [DEME][IM_{xx}] samples (0≤x≤4) at ambient conditions. In the inset the low Q portion is reported (covering the same Q range accessed by the SANS data set described in Figure 2).

View Article Online
DOI: 10.1039/C7CP01971H

similarly to other ILs bearing [IM_{xx}] anions (in particular for x=0, 1, 2), two peaks characterise the low Q portion (Q<2 Å^{-1}) of the X-ray diffraction patterns; these peaks are centred at approximately 0.8 and 1.2 Å^{-1} (Q_{II} and Q_{III}, respectively).[43,88–101] They have been shown in the past to be related to charge and close contact alternations, respectively [88,102]. On the other hand [DEME]-based ILs have been poorly investigated from the liquid state structure point of view and to our knowledge there are no X-ray scattering studies focused on the determination of liquid structure for this class of RTILs. Nevertheless, considering the short alkyl chain connected to the ammonium nitrogen in the [DEME] cation it is not surprising that at Q values below 0.6 Å^{-1}, no further diffraction feature occurs as due to the characteristic polar-apolar alternation that is commonly found in other ILs bearing a long alkyl chain [89,90,93,97,101]. It is noteworthy to remind that ILs based on the asymmetric anion [IM_{xy}] (with xy=14 and 24) have been found to show a featureless low Q X-ray diffraction pattern at ambient temperature, while a distinct low Q peak, centred at Q_I~0.4-0.45 Å^{-1}, emerged when decreasing temperature below 230 K[43]. This peak has been attributed to the fingerprint of fluorinated tails segregation and a related finding has been reported for Butylammonium Pentadecafluorooctanoate (BAOF) at 50°C (this salt is solid at ambient conditions and the segregation of the fluorinated tails is imposed by the rigid hydrogen bonded network established in the sample)[35,36]. These evidences so far have been puzzling ones: while the X-ray scattering experiments presented in reference [43] on a series of [IM_{xy}] (with xy=14 and 24) based ILs were collected at experimental conditions where the samples remained liquid or super-cooled liquid (i.e. no crystallization events could be detected in the whole explored temperature range), nevertheless it remained unexplained the reason why the low Q peak fingerprinting the fluorinated tails segregation appeared only at low temperature. Also, in the present selection of [DEME][IM_{xx}] samples, at least in the case where x=4, one would expect the existence of fluorinated tails segregation that is however not detected by the X-ray scattering spectrum.

The solution to this puzzling situation emerges when examining the series of [DEME][IM_{xx}] samples using Small Angle Neutron Scattering (SANS): in Figure 2 we report SANS data from these samples at ambient conditions. These data cover only a limited Q range as compared to the X-ray data set shown in Figure 1; nevertheless it can be appreciated the existence of the peak centred at Q_{II} (ca. 0.8 Å^{-1}), while Q_{III} is outside of the accessible Q range. These data indicate however that when probing [DEME][IM_{xx}] ILs with x≥3, a distinct shoulder or peak emerges over the incoherent background. The position of this peak (Q_I) is found to depend on x (vide infra) and falls at Q values where the X-ray pattern is completely featureless (see inset of Figure 1, where the same Q range is shown). The data shown in Figure 2 have been modelled assuming that peaks Q_I and Q_{II} can be described with two Gaussian functions and the background is a flat, incoherent, one. Figure 3 shows the resulting fits for [DEME][IM_{xx}], with x≥2 (fits of data sets for x=0 and 1 led to unreproducible results). The proposed model can efficiently account for the two observed diffraction features (Q_I and Q_{II}) and the characteristic sizes associated to these diffraction peaks (D_I and D_{II}, respectively) were extracted using the Bragg's law and are plotted in the inset of Figure 3, as a function of the anion's chain length, x. In this figure, together with D_I and D_{II}, we also report the corresponding value for D_{II} obtained by X-ray scattering: the latter nicely compares with the corresponding SANS quantity and shows very small x-dependence, in agreement with similar findings from other related systems (see e.g. reference [95]). On the other hand D_I shows a distinct x-dependence and, similarly to other related systems, this trend is linear with respect to the number of carbon atoms along the side chain. The slope of the line describing such a trend is 2.0 Å/CF_2 unit, similarly with the value obtained for the case of alkyl chains connected e.g. to imidazolium heads (1.96 Å/CF_2 unit for [$C_n$mim][IM_{11}], see ref. [89]). The low Q peaks positions in the case of alkyl chains connected either to asymmetric or to symmetric ions

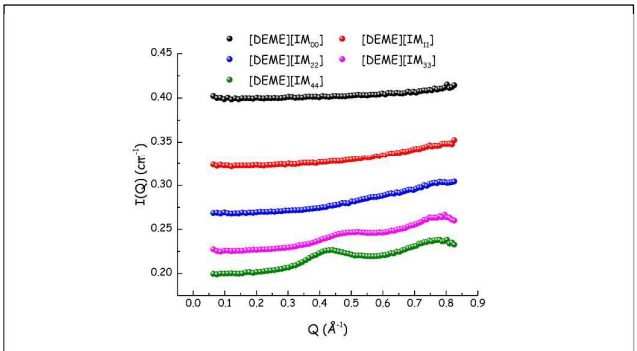

Figure 2. SANS data from the series of [DEME][IM_{xx}] samples (0≤x≤4) at ambient conditions.

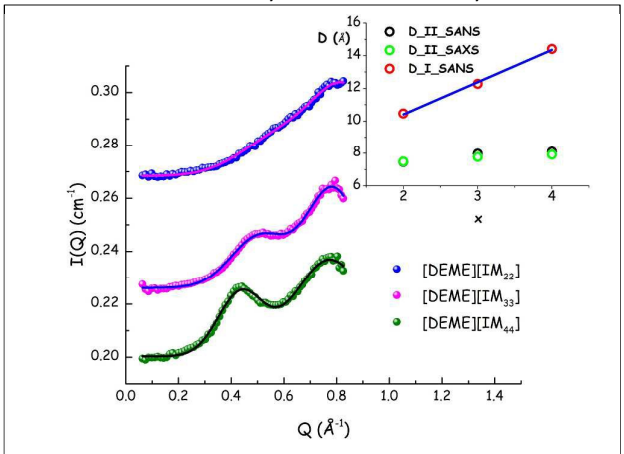

Figure 3. Fit of the SANS data from the series of [DEME][IM_{xx}] samples (2≤x≤4), using a model with two Gaussian functions and a flat background. In the inset the x dependence of the characteristic sizes obtained from SANS and SAXS data is reported. For the case of the low Q peak in the SANS data, Q_I, a linear fit is also shown.

View Article Online
DOI: 10.1039/C7CP01971H

(specifically in the case of asymmetrically and symmetrically substituted imidazolium salt, $[C_nmim][IM_{11}]$ and $[C_nC_nim][IM_{11}]$, respectively see refs. [95,103,104]) are located at similar positions: peak Q_I in asymmetric substituted cations is systematically located at slightly lower Q values than the same peak in the case of symmetrically substituted cations. Accordingly it makes sense the fact that the low Q peak observed in the present case of $[IM_{44}]$-based salt falls at a slightly larger Q value than the corresponding peak in the case of $[IM_{14}]$-based salts. [43]

The present set of SANS data provides then the first direct experimental evidence of the existence of structural heterogeneities related to the spatial segregation of fluorinated tails in FRTILs, in agreement with the proposal by Ferreira et al.[51]. Such clusters originate from the assembly of fluorous tails embedded into the polar three dimensional matrix that is formed by the charged moieties that interact through strong Coulombic interactions, in a way that is very similar to the spatial segregation of alkyl tails in more common RTILs. Previously experimental reports where low Q peaks originated from the segregation of fluorous tails, such as those presented in refs. [35,36], refer to situations where the presence of strong hydrogen bonding (HB) interactions between ions drives the mutual segregation of incompatible moieties: the relatively high melting point of BAOF witnesses the major role played by HB in affecting the morphology of this class of system that eventually perform as 'poor ionic liquids" even at temperatures higher than room conditions.[35] The present choice of RTILs ensures that they have interesting Λ vs η^{-1} trend, as reported in the Walden plot in ref. [45]; on the other hand, those data reflect the fact that upon elongating the fluorinated tails, a diminished ion diffusion is found, similarly to other related cases[105–107], fingerprinting the development of van der Waals interactions between side chains embedded into segregated clusters.

Molecular Dynamics simulations were conducted on two selected samples of the series $[DEME][IM_{xx}]$, namely on samples with x=1 and 4. While a full description of these studies together with a comparison with other members of the family will be presented in a different contribution in the near future, here we present salient results that are pertinent to the present focus of fluorous tails segregation. As anticipated above, the main tool to be used in order to experimentally identify the existence of fluorous clusters is a comparison between SAXS and SANS experimental patterns (compare Figures 1 and 2). Accordingly, after prolonged equilibration, Molecular Dynamics (MD) trajectories have been interrogated to extract X-ray and neutron weighted computed scattering functions, S(Q). Figure 4 shows a comparison between computed diffraction patterns for $[DEME][IM_{11}]$ and $[DEME][IM_{44}]$. It clearly emerges that the employed potentials

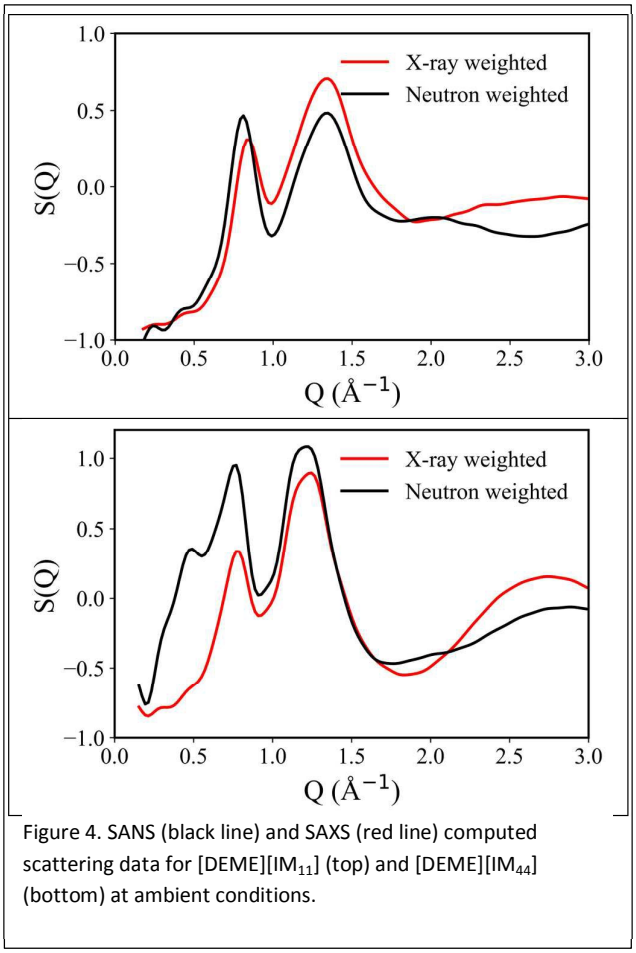

Figure 4. SANS (black line) and SAXS (red line) computed scattering data for $[DEME][IM_{11}]$ (top) and $[DEME][IM_{44}]$ (bottom) at ambient conditions.

are capable to grasp the main experimental finding of this study, i.e. the present simulation set highlights the existence of the low Q peak in the SANS pattern from $[DEME][IM_{44}]$ that is not present in its SAXS pattern. Such a result implies that we can safely interrogate these simulations in order to extract structural information at atomistic level to rationalise the experimental evidences. For illustration's sake, we show in Figure 5 a representative snapshot from the MD simulation of $[DEME][IM_{44}]$, where we differently coloured the polar (the whole cation and the central part of the anion, i.e. the $N(SO_2)_2$ moiety) and the apolar (the fluorinated tails) moieties. The segregation of polar vs apolar moieties clearly emerges from this snapshot, identifying a spatial scale of the order of several Å that has a counterpart in the low Q peak observed both experimentally and computationally. Following well established approaches to interpret these features[47,88,108,109], we decomposed the computed SAXS and SANS patterns into contributions that help in understanding the physical origin of the different diffraction features.

View Article Online
DOI: 10.1039/C7CP01971H

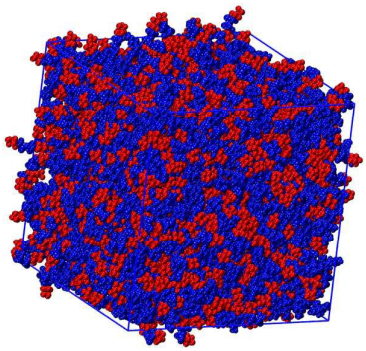

Figure 5. Representative snapshot from [DEME][IM_{44}] simulation at ambient conditions. Polar moieties are red coloured and apolar ones are blue colour.

Figure 6 reports the ionic partitioning of S(Q): the different contributions to S(Q) arising from correlations between cation-cation, anion-anion and cation-anion are separately shown for both [DEME][IM_{11}] (top) and [DEME][IM_{44}] (bottom). Analogously to other related studies these graphs clearly show that the peak centred at Q_{II} (approx. 0.8 $Å^{-1}$) originates from the superposition of two peaks with positive amplitude (the ones associated to the correlations between ions of the same sign, i.e. cation-cation and anion-anion) and a peak with negative amplitude (the one associated to correlations between ions of opposite sign, i.e. cation-anion): this is the typical fingerprint of alternating charged layers that is found ubiquitously in ILs systems and leads to the presence of the peak centred at Q_{II}.

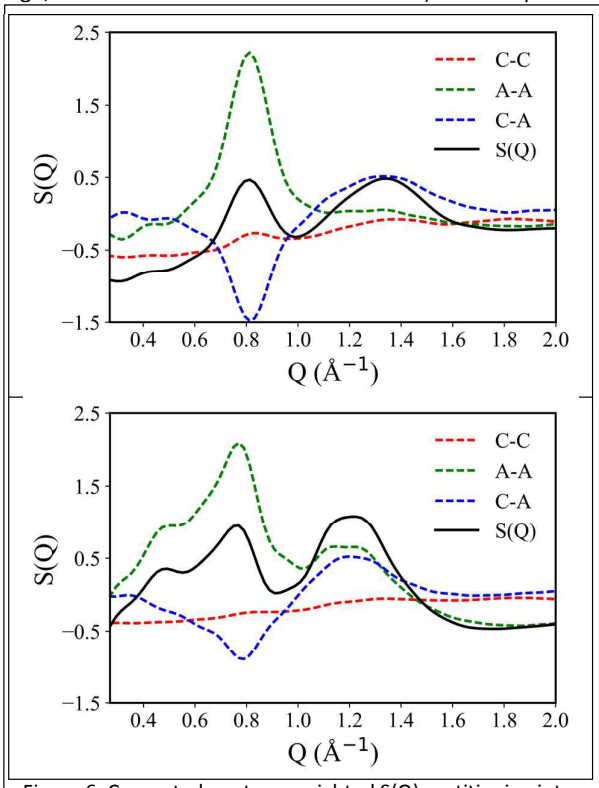

Figure 6. Computed neutron-weighted S(Q) partitioning into cation-cation (C-C), anion-anion (A-A) and cation-anion (C-A) components for [DEME][IM_{11}] (top) and [DEME][IM_{44}] (bottom).

On the other hand, in order to rationalise the nature of the low Q peak centred at the Q_I position, a different partitioning of the neutron weighted S(Q) must be used. In particular several studies earlier showed that the low Q scattering features that is ubiquitous in ILs bearing a long enough apolar tail is the fingerprint of polar/apolar alternation characterising the structure at the bulk level. [47,88,108,109] (but also [110] for the case of non-ionic compounds) Accordingly Figure 7 reports a decomposition of neutron weighted S(Q) in terms of components arising from polar-polar, apolar-apolar and polar-apolar (P-P, A-A and P-A, respectively) structural correlations for the case of [DEME][IM_{44}]. Inspection of this figure allows detecting the existence of two positive amplitude peaks (associated to P-P and A-A correlations) and a negative amplitude peak (associated to P-A correlations) whose combination delivers the low Q peak centred at ca. 0.5 $Å^{-1}$. This corresponds to the expected behaviour on the basis of previous studies, where the apolar component was represented by an alkyl chain. In the present case, it is the fluorous moieties that alternate with the polar portions and lead to the development of a distinct low Q peak. Overall this analysis provides conclusive confirmation on the nature of the low Q peak that emerges in [DEME][IM_{xx}], with increasing x, as the fingerprint of nano-scale domains of fluorous moieties, whose size grows with increasing chain length.

Finally, the results of some NMR experiments are here reported and discussed as a support to the previous sections. One important NMR tool useful to investigate local order and segregation phenomena in ILs is the intermolecular NOE. The fundamental theory behind the use of intermolecular NOEs in ionic liquids and the interpretation of NOE data are undergoing rapid evolution: The group of Weingärtner[111] published a detailed theoretical model for the evaluation of the spectral density functions for homonuclear and heteronuclear NOE in

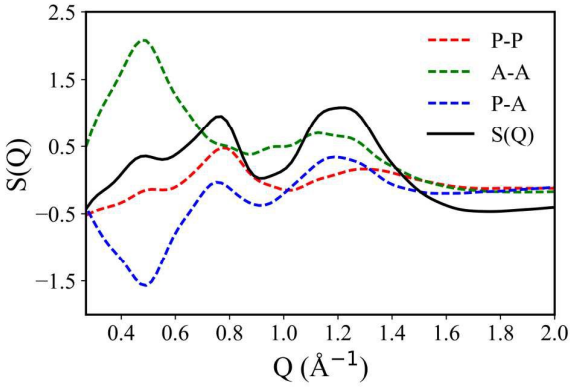

Figure 7. Computed neutron-weighted S(Q) partitioning into polar-polar (P-P), apolar-apolar (A-A) and polar-apolar (P-A) components for [DEME][IM_{44}].

View Article Online
DOI: 10.1039/C7CP01971H

model ionic liquid. One of the main conclusions was that intermolecular NOE is dominated by long range effects extending beyond the 4-5 Å threshold commonly considered for vanishing intramolecular NOE. Thus, intermolecular NOEs are expected to spot on solvation shells beyond the first one in the case the Larmor frequencies of the interacting nuclei are very close, as for the homonuclear NOE and heteronuclear {^{1}H–^{19}F} NOE. Accordingly, the intermolecular NOE data may account for nanometer-scale structural motives too, thus providing an invaluable structural tool complementary to X-ray and neutron scattering methods. In a previous paper on triphilic ILs containing asymmetric IM_{14} and IM_{24} anions, we showed that homonuclear {^{19}F–^{19}F} NOE could give direct proof of the existence of perfluorocarbons domains[43]. Therein, the F···F distances of the fluorinated moieties calculated at DFT level allowed us to discriminate the observed {^{19}F–^{19}F} NOEs in intra- and intermolecular, the latter being consistent with the formation of fluorous domains, by using the criterium of the 4-5 Å threshold. The application of such protocol in the present cases is less straightforward because anions' symmetry (see Scheme 1, ESI) introduces magnetic equivalence, thus reducing the number of NMR signals. In the case of IM_{44}, the longest F···F distance is the one between terminal CF_3 and first CF_2 (e.g. CF_3(1) and CF_2(4), see Scheme 1 (ESI) for atom numbering). The average distance calculated for the all trans conformation of the nonafluorobutyl chain is about 4.9 Å, namely on the border between the distance providing either intra- or intermolecular NOEs. Experimentally, the {^{19}F–^{19}F} NOESY determined on [DEME][IM_{44}] showed a cross-peak connecting CF_3(1) to CF_2(4), along with other expected intramolecular contacts. The presence of the CF_3(1) / CF_2(4) NOE contact is consistent with the existence of segregated apolar domains of the fluorous tails, although it is not a conclusive argument. The contacts between the polar and apolar moieties have been explored by a systematic {^{1}H–^{19}F} HOESY determined on all the ILs examined in this work. For each of them the {^{1}H–^{19}F} NOE build-up curves (e.g. NOE intensity vs mixing time) were collected and fitted to obtain quantitative NOE intensities. The detailed discussion of these results is beyond the goals of the present work and will be detailed elsewhere. Suffice to anticipate here two findings: i) the systematic change of the {^{1}H–^{19}F} NOE profile with increasing length of the fluorinated chains, and ii) a paradigmatic case concerning [DEME][IM_{11}] and [DEME][IM_{44}]. The {^{1}H–^{19}F} NOE profile related to the CF_3 groups of the alkyl chains of [IM_{xx}] anions with x=1, 2, 3 and 4 with all the H atoms of the corresponding DEME cation is reported in Figure 9.

The CF_3 group was chosen because it is the end-of-chain group for all the anions and, as such, the ideal probe for the interdomain contacts.

The NOE profile for [DEME][IM_{11}] is here considered the reference for IL with no segregation of polar and apolar domains. The other profiles are proposed as a fingerprint of the anion-cation organisation as a function of the chain length. The picture clearly emerging from the profiles is that of a progressive and systematic change of the ions organisation with increasing length of the perfluoroalkyl tail. More specifically, in the economy of the characterisation of the segregation of the apolar chains, a paradigmatic case is presented now, based on a comparison between [DEME][IM_{11}] and [DEME][IM_{44}]. In both cases we were able to detect a NOE contact between CF_3 and CH_3(1), signifying the existence of intermolecular interactions. In the case of [DEME][IM_{11}], such contact can be ascribed mainly to the formation of anion-cation aggregates driven by Coulombic interactions. Figure 9 shows the radial distribution function for the F···H distance between the functional groups mentioned above, derived from the MD trajectories. The pattern shown for [DEME][IM_{11}] (red curve) is characteristic of the charge alternation, with the absolute maximum due to the first neighbours at ca. 5 Å. Conversely, the curve for [DEME][IM_{44}] (blue curve) shows a shallow, single maximum at about 9 Å, suggesting that the terminal CF_3 groups of the nonafluorobutyl chains interact with the polar domain at much larger distances, consistently with the picture of segregation of the fluorine-containing chains in an apolar domains adjacent to the polar ones, as depicted in Figure 5.

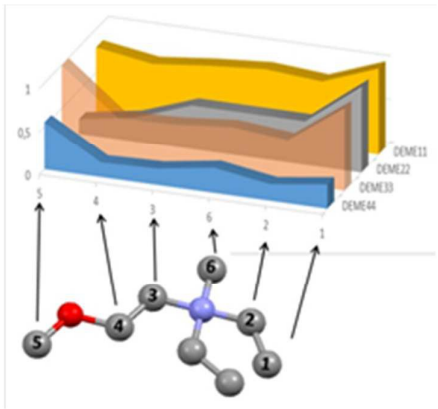

Figure 8. The plot reports the quantitative, normalized NOE between the CF_3 group of each anion (secondary x-axis) with all the H atoms of the cation. The y-axis shows the normalized NOE intensity, the x-axis contains the H atom numbers for the DEME structure defined in Scheme 1 (ESI). For clarity, the x-axis numbers can be associated to the cation structure just observing the ball-and-stick model below the x-axis. The arrows are a guide for the eyes.

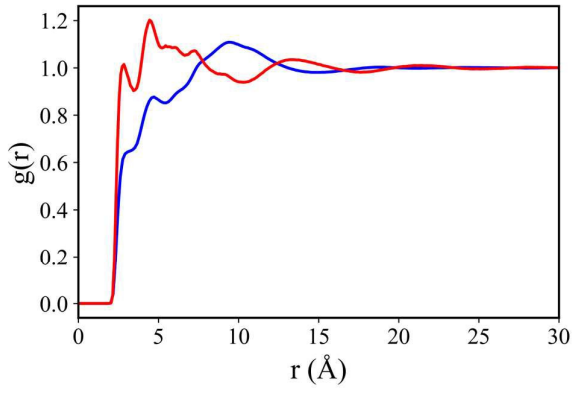

Figure 9. Profile of the radial distribution function of CF_3···CH_3(1) distances for [DEME][IM_{11}] (red line) and [DEME][IM_{44}] (blue line).

View Article Online
DOI: 10.1039/C7CP01971H

Conclusion

This study allows detecting the existence of distinct structural heterogeneities in the mesoscopic scale that originate from the spatial segregation of fluorous tails in FRTILs. We stress that X-ray scattering turns out to be not the ideal probe to access such structural feature, due to contrast reasons. On the other hand neutron scattering allows probing in the most direct way the existence of a diffraction feature that nicely prompts for the existence of fluorous domains in the nm scale. Similarly to the case of conventional RTILs with alkyl chains, the size of the apolar domains linearly depends on the chain length. NMR evidences further support this segregation model and Molecular Dynamics simulations allow determining unambiguously the polar vs apolar alternation mechanism that drives the formation of these segregated morphology.

We can envisage the preferential dissolution of fluorous or greenhouse gases into these fluorous domains that might prompt for more accurate studies aiming at fully exploiting the opportunities provided by FRTILs in fields such as gas capturing, biphasic fluorous synthesis etc.

Acknowledgements.

AT acknowledges Dr. B. Aoun for his kind and competent assistance in using beamline 11-ID-C at APS. This research used resources of the Advanced Photon Source, a U.S. Department of Energy (DOE) Office of Science User Facility operated for the DOE Office of Science by Argonne National Laboratory under Contract No. DE-AC02-06CH11357.

This work was partly supported by the Japan Society for the Promotion of Science (JSPS) KAKENHI Grant Numbers JP22685015 and JP25288041.

Notes and references

1 A. B. Lindstrom, M. J. Strynar and E. L. Libelo, *Environ. Sci. Technol.*, 2011, **45**, 7954–7961.
2 J. G. Riess, *Curr. Opin. Colloid Interface Sci.*, 2009, **14**, 294–304.
3 M. P. Krafft and J. G. Riess, *Chem. Rev.*, 2009, **109**, 1714–92.
4 J. G. Riess, *Chem. Rev.*, 2001, **101**, 2797–2920.
5 J. G. Riess, *Tetrahedron*, 2002, **58**, 4113–4131.
6 Q. Jochyms, E. Mignard and J. M. Vincent, *J. Fluor. Chem.*, 2015, **177**, 11–18.
7 E. de Wolf, G. van Koten and B.-J. Deelman, *Chem. Soc. Rev.*, 1999, **28**, 37–41.
8 R. H. Fish, *Chem. - A Eur. J.*, 1999, **5**, 1677–1680.
9 B. Cornils, *Angew. Chemie Int. Ed. English*, 1997, **36**, 2057–2059.
10 H. R. Hobbs and N. R. Thomas, *Chem. Rev.*, 2007, **107**, 2786–2820.
11 E. G. Hope and A. M. Stuart, *J. Fluor. Chem.*, 1999, **100**, 75–83.
12 J. . Gladysz and D. P. Curran, *Tetrahedron*, 2002, **58**, 3823–3825.
13 I. T. Horvath and J. Rabai, *Science (80-.).*, 1994, **266**, 72–75.
14 I. T. Horvath, *Acc. Chem. Res.*, 1998, **31**, 641–650.
15 a Studer, S. Hadida, R. Ferritto, S. Y. Kim, P. Jeger, P. Wipf and D. P. Curran, *Science*, 1997, **275**, 823–826.
16 Z. Luo, Q. Zhang, Y. Oderaotoshi and D. P. Curran, *Science*, 2001, **291**, 1766–9.
17 W. Zhang, *Chem. Rev.*, 2004, **104**, 2531–2556.
18 W. Zhang, *Tetrahedron*, 2003, **59**, 4475–4489.
19 C. Yang, X. Wang and M. A. Omary, *J. Am. Chem. Soc.*, 2007, **129**, 15454–15455.
20 A. M. A. Dias, J. C. Pa, I. M. Marrucho and L. F. Vega, *J. Phys. Chem. B*, 2004, **108**, 1450–1457.
21 A. M. A. Dias, R. P. Bonifácio, I. M. Marrucho, A. A. H. Pádua and M. F. Costa Gomes, *Phys. Chem. Chem. Phys.*, 2003, **5**, 543–549.
22 A. B. Pereiro, J. M. M. Araújo, S. Martinho, F. Alves, S. Nunes, A. Matias, C. M. M. Duarte, L. P. N. Rebelo and I. M. Marrucho, *ACS Sustain. Chem. Eng.*, 2013, **1**, 427–439.
23 J. H. Davis, K. J. Forrester and T. Merrigan, *Tetrahedron Lett.*, 1998, **39**, 8955–8958.
24 T. L. Merrigan, E. D. Bates, S. C. Dorman and J. H. Davis Jr., *Chem. Commun.*, 2000, 2051–2052.
25 D. Almantariotis, T. Gefflaut, A. A. H. Pádua, J.-Y. Coxam and M. F. Costa Gomes, *J. Phys. Chem. B*, 2010, **114**, 3608–3617.
26 G. D. Smith, O. Borodin, J. J. Magda, R. H. Boyd, Y. Wang, J. E. Bara, S. Miller, D. L. Gin and R. D. Noble, *Phys. Chem. Chem. Phys.*, 2010, **12**, 7064.
27 D. Almantariotis, A. S. Pensado, H. Q. N. Gunaratne, C. Hardacre, A. A. H. Pádua, J.-Y. Coxam and M. F. Costa Gomes, *J. Phys. Chem. B*, 2017, **121**, 426–436.
28 H. Weber, O. Hollóczki, A. S. Pensado and B. Kirchner, *J. Chem. Phys.*, 2013, **139**, 84502.
29 D. H. Zaitsau, A. V. Yermalayeu, S. P. Verevkin, J. E. Bara and D. A. Wallace, *Thermochim. Acta*, 2015, **622**, 38–43.
30 O. Hollóczki, M. Macchiagodena, H. Weber, M. Thomas, M. Brehm, A. Stark, O. Russina, A. Triolo and B. Kirchner, *ChemPhysChem*, 2015, **16**, 3325–3333.
31 H. Xue, R. Verma and J. M. Shreeve, *J. Fluor. Chem.*, 2006, **127**, 159–176.
32 H. Xue and J. M. Shreeve, *Eur. J. Inorg. Chem.*, 2005, 2573–2580.
33 J. J. Tindale and P. J. Ragogna, *Chem. Commun.*, 2009, 1831.
34 Y. Tsukada, K. Iwamoto, H. Furutani, Y. Matsushita, Y. Abe, K. Matsumoto, K. Monda, S. Hayase, M. Kawatsura and T. Itoh, *Tetrahedron Lett.*, 2006, **47**, 1801–1804.
35 Y. Shen, D. F. Kennedy, T. L. Greaves, A. Weerawardena, R. J. Mulder, N. Kirby, G. Song and C. J. Drummond, *Phys. Chem. Chem. Phys.*, 2012, **14**, 7981–92.
36 J. J. Hettige, J. C. Araque and C. J. Margulis, *J. Phys. Chem. B*, 2014, **118**, 12706–16.
37 S. Martinho, J. M. M. Araújo, L. P. N. Rebelo, a. B. Pereiro and I. M. Marrucho, *J. Chem. Thermodyn.*, 2013, **64**, 71–79.
38 A. B. Pereiro, M. J. Pastoriza-Gallego, K. Shimizu, I. M. Marrucho, J. N. C. Lopes, M. M. Piñeiro and L. P. N. Rebelo,

View Article Online
DOI: 10.1039/C7CP01971H

J. Phys. Chem. B, 2013, **117**, 10826–10833.
39 N. S. M. Vieira, P. M. Reis, K. Shimizu, O. a. Cortes, I. M. Marrucho, J. M. M. Araújo, J. M. S. S. Esperança, J. N. C. Lopes, a. B. Pereiro and L. P. N. Rebelo, *RSC Adv.*, 2015, **5**, 65337–65350.
40 A. R. R. Teles, H. Correia, G. J. Maximo, L. P. N. Rebelo, M. G. Freire, A. B. Pereiro and J. A. P. Coutinho, *Phys. Chem. Chem. Phys.*, 2016, **18**, 25741–25750.
41 G. B. Appetecchi, M. Montanino, M. Carewska, M. Moreno, F. Alessandrini and S. Passerini, *Electrochim. Acta*, 2011, **58**, 1300–1307.
42 S. Jeremias, M. Carewska, L. Conte, S. Passerini and G. B. Appetecchi, *RSC Adv.*, 2013, **3**, 17755.
43 O. Russina, F. Lo Celso, M. Di Michiel, S. Passerini, G. B. Appetecchi, F. Castiglione, A. Mele, R. Caminiti and A. Triolo, *Faraday Discuss.*, 2013, **167**, 499.
44 F. Castiglione, A. Famulari, G. Raos, S. V Meille, A. Mele, G. B. Appetecchi and S. Passerini, *J. Phys. Chem. B*, 2014, **118**, 13679–13688.
45 Y. Yoshida and G. Saito, *Phys. Chem. Chem. Phys.*, 2011, **13**, 20302.
46 T. Mochida, Y. Funasako, T. Inagaki, M. J. Li, K. Asahara and D. Kuwahara, *Chem. - A Eur. J.*, 2013, **19**, 6257–6264.
47 B. Wu, Y. Yamashita, T. Endo, K. Takahashi and E. W. Castner, *J. Chem. Phys.*, 2016, **145**, 244506.
48 H. Weiss, J. Mars, H. Li, G. Kircher, O. Ivanova, A. Feoktystov, O. Soltwedel, M. Bier and M. Mezger, *J. Phys. Chem. B*, 2017, **121**, 620–629.
49 C. Liu, F. Xu, S. Feng, L. Zheng, H. Zhang, W. Feng, X. Huang, M. Armand, J. Nie and Z. Zhou, *Electrochim. Acta*, 2013, **99**, 262–272.
50 D. R. MacFarlane, M. Forsyth, P. C. Howlett, M. Kar, S. Passerini, J. M. Pringle, H. Ohno, M. Watanabe, F. Yan, W. Zheng, S. Zhang and J. Zhang, *Nat. Rev. Mater.*, 2016, **1**, 15005.
51 M. L. Ferreira, M. J. Pastoriza-Gallego, J. M. M. Araújo, J. N. Canongia Lopes, L. P. N. Rebelo, M. M. Piñeiro, K. Shimizu and A. B. Pereiro, *J. Phys. Chem. C*, 2017, acs.jpcc.7b00516.
52 Y. Imai, H. Abe, T. Goto, Y. Yoshimura, S. Kushiyama and H. Matsumoto, *J. Phys. Chem. B*, 2008, **112**, 9841–9846.
53 Y. Imai, H. Abe, T. Goto, Y. Yoshimura, Y. Michishita and H. Matsumoto, *Chem. Phys.*, 2008, **352**, 224–230.
54 Y. Yoshimura, T. Goto, H. Abe and Y. Imai, *J. Phys. Chem. B*, 2009, **113**, 8091–5.
55 H. Abe, Y. Imai, T. Goto, Y. Yoshimura, M. Aono, T. Takekiyo, H. Matsumoto and T. Arai, *Metall. Mater. Trans. A*, 2009, **41**, 1137–1143.
56 Y. Imai, H. Abe, T. Goto, T. Takekiyo and Y. Yoshimura, *High Press. Res.*, 2009, **29**, 536–541.
57 H. Abe, Y. Yoshimura, Y. Imai, T. Goto and H. Matsumoto, *J. Mol. Liq.*, 2009, **150**, 16–21.
58 M. Aono, Y. Imai, Y. Ogata, H. Abe, T. Goto, Y. Yoshimura, T. Takekiyo, H. Matsumoto and T. Arai, *Metall. Mater. Trans. A*, 2010, **42**, 37–40.
59 T. Mochida, Y. Funasako, T. Inagaki, M. Li, K. Asahara and D. Kuwahara, *Chem. - A Eur. J.*, 2013, **19**, 6257–6264.
60 P. Bonhôte, A.-P. Dias, M. Armand, N. Papageorgiou, K. Kalyanasundaram and M. Grätzel, *Inorg. Chem.*, 1996, **35**, 1168.
61 H. Matsumoto, N. Terasawa, T. Umecky, S. Tsuzuki, H. Sakaebe, K. Asaka and K. Tatsumi, *Chem. Lett.*, 2008, **37**, 1020–1021.
62 Z. Bin Zhou, H. Matsumoto and K. Tatsumi, *Chem. - A Eur. J.*, 2005, **11**, 752–766.
63 A. Lewandowski and A. Świderska-Mocek, *J. Power Sources*, 2009, **194**, 601–609.
64 T. Sato, G. Masuda and K. Takagi, *Electrochim. Acta*, 2004, **49**, 3603–3611.
65 K. Yuyama, G. Masuda, H. Yoshida and T. Sato, *J. Power Sources*, 2006, **162**, 1401–1408.
66 K. Ueno, H. Shimotani, H. Yuan, J. Ye, M. Kawasaki and Y. Iwasa, *J. Phys. Soc. Japan*, 2014, **83**, 1–16.
67 K. Shimizu, A. A. Freitas and J. N. Canongia Lopes, *J. Mol. Liq.*, 2017, **226**, 28–34.
68 X. Qiu, J. W. Thompson and S. J. L. Billinge, *J. Appl. Crystallogr.*, 2004, **37**, 678.
69 U. Keiderling and A. Wiedenmann, *Phys. B*, 1995, **213–214**, 895–897.
70 R. Gilles, U. Keiderling, P. Strunz, A. Wiedenmann and H. Fuess, *Mater. Sci. Forum*, 2000, **321–3**, 264–269.
71 U. Keiderling, *Appl. Phys. A Mater. Sci. Process.*, 2002, **74**, s1455–s1457.
72 T. M. Alam, D. M. Pedrotty and T. J. Boyle, *Magn. Reson. Chem.*, 2002, **40**, 361–365.
73 S.-S. Hou, J.-K. Tzeng and M.-H. Chuang, *Soft Matter*, 2010, **6**, 409–415.
74 Y. Lingscheid, S. Arenz and R. Giernoth, *ChemPhysChem*, 2012, **13**, 261–266.
75 B. Hess, C. Kutzner, D. Van Der Spoel and E. Lindahl, *J. Chem. Theory Comput.*, 2008, **4**, 435–447.
76 D. Van Der Spoel, E. Lindahl, B. Hess, G. Groenhof, A. E. Mark and H. J. C. Berendsen, *J. Comput. Chem.*, 2005, **26**, 1701–1718.
77 J. N. Canongia Lopes, J. Deschamps and A. A. H. Padua, *J. Phys. Chem. B*, 2004, **108**, 2038–2047.
78 W. L. Jorgensen, D. S. Maxwell and J. Tirado-Rives, *J. Am. Chem. Soc.*, 1996, **118**, 11225–11236.
79 K. Shimizu, D. Almantariotis, M. F. C. Gomes, A. A. H. Pádua and J. N. Canongia Lopes, *J. Phys. Chem. B*, 2010, **114**, 3592–3600.
80 J. N. Canongia Lopes and A. A. H. Padua, *J. Phys. Chem. B*, 2004, **108**, 16893–16898.
81 J. N. Canongia Lopes and A. A. H. Pádua, *Theor. Chem. Acc.*, 2012, **131**, 1129.
82 C. E. S. Bernardes and A. Joseph, *J. Phys. Chem. A*, 2015, **119**, 3023–34.
83 G. Bussi, D. Donadio and M. Parrinello, *J. Chem. Phys.*, 2007, **126**, 14101.
84 M. Parrinello and A. Rahman, *J. Appl. Phys.*, 1981, **52**, 7182–7190.
85 T. Darden, D. York and L. Pedersen, *J. Chem. Phys.*, 1993, **98**, 10089.
86 U. Essmann, L. Perera, M. L. Berkowitz, T. Darden, H. Lee and L. G. Pedersen, *J Chem Phys*, 1995, **103**, 8577–8593.

View Article Online
DOI: 10.1039/C7CP01971H

87 J. D. Hunter, *Comput. Sci. Eng.*, 2007, **9**, 90–95.
88 H. K. Kashyap, J. J. Hettige, H. V. R. Annapureddy and C. J. Margulis, *Chem. Commun. (Camb).*, 2012, **48**, 5103–5.
89 O. Russina, A. Triolo, L. Gontrani, R. Caminiti, D. Xiao, L. G. Hines Jr, R. A. Bartsch, E. L. Quitevis, N. V. Plechkova, K. R. Seddon, N. Pleckhova, K. R. Seddon, N. V. Plechkova, K. R. Seddon and L. G. H. Jr, *J. Phys. Condens. Matter*, 2009, **21**, 424121.
90 C. S. Santos, N. S. Murthy, G. a. Baker and E. W. Castner, *J. Chem. Phys.*, 2011, **134**, 1211011–4.
91 K. Fujii, S. Seki, S. Fukuda, T. Takamuku, S. Kohara, Y. Kameda, Y. Umebayashi and S. Ishiguro, *J. Mol. Liq.*, 2008, **143**, 64–69.
92 K. Fujii, Y. Soejima, Y. Kyoshoin, S. Fukuda, R. Kanzaki, Y. Umebayashi, T. Yamaguchi, S. Ishiguro and T. Takamuku, *J. Phys. Chem. B*, 2008, **112**, 4329.
93 K. Fujii, R. Kanzaki, T. Takamuku, Y. Kameda, S. Kohara, M. Kanakubo, M. Shibayama, S. Ishiguro and Y. Umebayashi, *J. Chem. Phys.*, 2011, **135**, 244502.
94 B. Wu, H. Shirota, S. Lall-Ramnarine and E. W. Castner, *J. Chem. Phys.*, 2016, **145**, 114501.
95 M. A. A. Rocha, C. M. S. S. Neves, M. G. Freire, O. Russina, A. Triolo, J. a. P. P. Coutinho and L. M. N. B. F. Santos, *J. Phys. Chem. B*, 2013, **117**, 10889–10897.
96 E. Bodo, L. Gontrani, R. Caminiti, N. V. Plechkova, K. R. Seddon and A. Triolo, *J. Phys. Chem. B*, 2010, **114**, 16398–16407.
97 A. Triolo, O. Russina, B. Fazio, G. B. Appetecchi, M. Carewska and S. Passerini, *J. Chem. Phys.*, 2009, **130**, 1645211–6.
98 A. Triolo, O. Russina, H.-J. Bleif and E. Di Cola, *J. Phys. Chem. B*, 2007, **111**, 4641–4.
99 O. Russina and A. Triolo, *Faraday Discuss.*, 2012, **154**, 97–109.
100 O. Russina, A. Triolo, L. Gontrani and R. Caminiti, *J. Phys. Chem. Lett.*, 2012, **3**, 27–33.
101 O. Russina, F. Lo Celso, N. V. Plechkova and A. Triolo, *J. Phys. Chem. Lett.*, 2017, 1197–1204.
102 K. Shimizu, C. E. S. Bernardes and J. N. Canongia Lopes, *J. Phys. Chem. B*, 2014, **118**, 567–576.
103 D. Xiao, L. G. Hines, S. Li, R. A. Bartsch, E. L. Quitevis, O. Russina, A. Triolo and L. G. Hines Jr., *J. Phys. Chem. B*, 2009, **113**, 6426–33.
104 W. Zheng, A. Mohammed, L. G. Hines, D. Xiao, O. J. Martinez, R. a Bartsch, S. L. Simon, O. Russina, A. Triolo and E. L. Quitevis, *J. Phys. Chem. B*, 2011, **115**, 6572–6584.
105 H. Tokuda, K. Hayamizu, K. Ishii, M. A. B. H. Susan and M. Watanabe, *J. Phys. Chem. B*, 2005, **109**, 6103–10.
106 H. Tokuda, S. Tsuzuki, M. A. B. H. Susan, K. Hayamizu and M. Watanabe, *J. Phys. Chem. B*, 2006, **110**, 19593–19600.
107 Y. Yoshida, O. Baba, C. Larriba and G. Saito, *J. Phys. Chem. B*, 2007, **111**, 12204–12210.
108 C. S. Santos, H. V. R. Annapureddy, N. S. Murthy, H. K. Kashyap, E. W. Castner and C. J. Margulis, *J. Chem. Phys.*, 2011, **134**, 64501.
109 J. C. Araque, J. J. Hettige and C. J. Margulis, *J. Phys. Chem. B*, 2015, **119**, 12727–12740.
110 F. Lo Celso, B. Aoun, A. Triolo and O. Russina, *Phys. Chem. Chem. Phys.*, 2016, **18**, 15980–15987.
111 S. Gabl, O. Steinhauser and H. Weingärtner, *Angew. Chemie Int. Ed.*, 2013, **52**, 9242–9246.

View Article Online
DOI: 10.1039/C7CP01971H

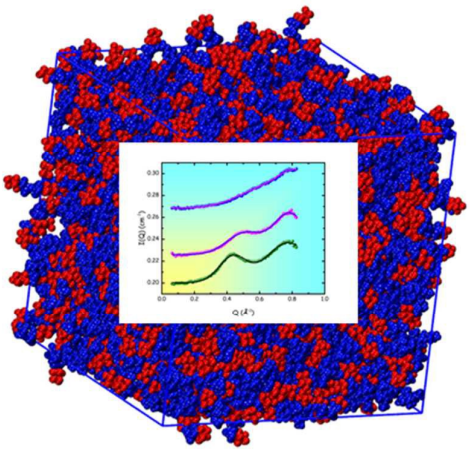

Neutron Scattering patterns reveal fluorinated nano-scale domains segregation in fluorinated Room Temperature Ionic Liquids.